A Robust High-Strength Multi-Surface Rapid UV-Curable Payload Installation System for Generic Multirotors via Impact Delivery

Ryan Lim [ID], Jeck Tan [ID], Matthew Ng [ID], Hong Yee Low, and Shaohui Foong [ID], *Member, IEEE*

Abstract—This letter details the design and development of a novel 3D-printed, lightweight and rapid-curing automated payload installation system for aerial robots, using a 3D printed resin-filled adhesive carrier tile (ACT). Its structure is designed to fracture and disperse ultraviolet (UV) curable resin on impact, delivered with a lightweight spring-driven impactor that rams the tile against a target surface. The dispersed resin is then cured with UV light. Shear-testing experiments with 40×40 mm ACTs across common building materials, surface conditions and roughness demonstrate loading exceeding 900 N only after 10 seconds of curing, showcasing the strength, robustness and speed of the proposed system. Automated payload installation experiments show potential for applications requiring strong and permanent bonds to wall structures, such as sensor payloads or tether points within urban environments. To the authors' knowledge, this is the first work employing wet UV adhesives for payload installation via multirotors.

Index Terms—Aerial systems: applications, mechanism design, aerial payload installation, multi-material 3d printing.

I. INTRODUCTION

NATURE contains many ingenious strategies for plant seed dispersal. Seed pods of *C. Hirsuta* rupture and elastically disperse seeds on contact (e.g. animal grazing) [1], while pods in *R. tuberosa* explode to release seeds due to weakening of seam tissue on water contact [2]. Other times, ballistic dispersal is insufficient. The parasitic Australian mistletoe *A. quandang* uses the mistletoebird *Dicaeum hirundinaceum* as a vector to deliver seeds onto host trees via mechanical adhesion. A sticky glue-like coating causes seeds to adhere to the bird on waste excretion, to which the bird responds by wiping the offending seeds against said host trees [3].

These strategies employed for targeted release and delivery piqued the authors' interest for aerial payload installation applications. For example, [4] used microdrones to install hooks for opening doors with ground reaction forces. In [5], bird diverters

were installed onto high-voltage powerlines with drones. [6] details a gravity-driven grappling system for installing payloads onto pole-like structures.

While researchers have developed numerous aerial vehicle capabilities for manipulation and/or payload delivery, such as valve-turning [7], perching [8], wall climbing [9] [10], inspection [11] [12] and wall drilling [13] [14], works on aerial payload installation are sparse in comparison. Furthermore, the aforementioned examples of payload installation involve structures with geometrical features amenable to hooking, grasping or impingement; namely (1) door handles, (2) powerlines and (3) poles, features which not all installation targets possess. Counter-examples include flat walls and other targets (e.g. trees or pillars), which are too large for manipulators (e.g. grippers, arms, etc.) on smaller vehicles to grasp properly.

Such targets are commonplace in urban and natural settings, hence solving this problem would greatly expand the scope of targets for aerial payload installation. We thus propose a nature-inspired UV resin payload installation system (URPIS) targeting large vertical flat surfaces, using UV-cured wet adhesives for aerial robots.

Several characteristics make URPIS suitable for multirotors. Firstly, complicated mechanisms for creating reaction forces (e.g. vacuum system in [14]) are avoided due to its low continuous force requirements. Secondly, re-use of primary flight motors for structurally-efficient perching reduces overall size, weight and power requirements [15]. Lasly, the chosen adhesive's general-purpose formulation lends it well to a variety of installation surfaces.

To the authors' knowledge, this is the first work employing UV-curable wet adhesives for payload installation using multirotors (see Fig. 1). The main contributions of this letter are:

- Conceptualisation, design and characterisation of a lightweight 3D-printed adhesive carrier tile (ACT) and impactor mechanism collectively known as URPIS, for payload installation applications using multirotors.
- Integration of a passive wall brace and heuristic-based wall detection with URPIS for automated deployment via multirotors as a demonstration of feasibility.

II. UV RESIN PAYLOAD INSTALLATION SYSTEM (URPIS) CONCEPTUALISATION

A. Concept of Operation

URPIS has 2 main constituents: (1) A UV resin-filled Adhesive Carrier Tile (ACT) and (2) Impactor Mechanism (IM). The
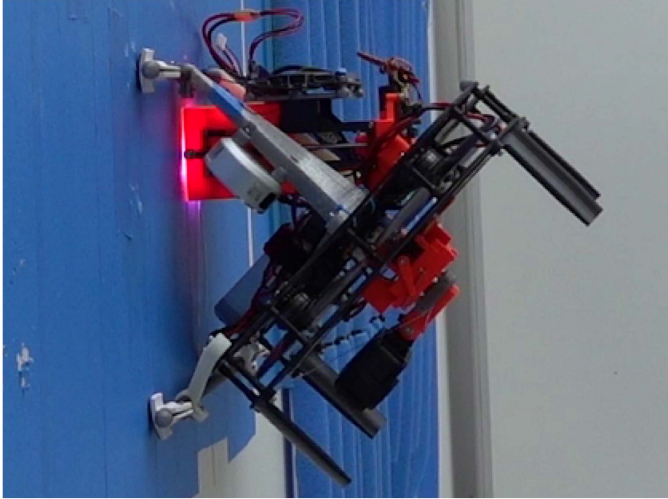
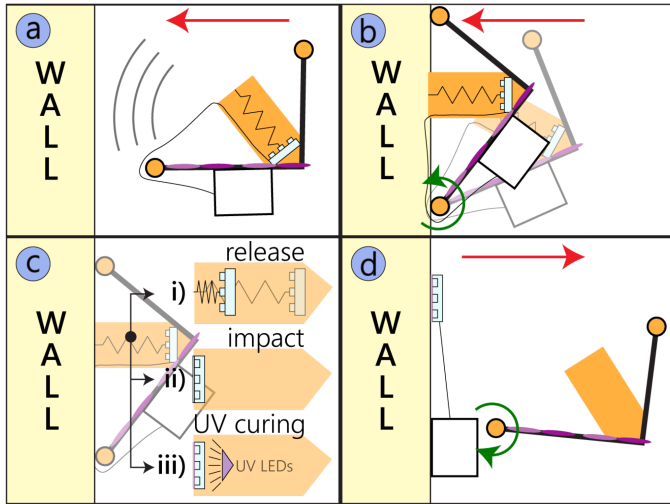Fig. 1.   System perched on wall during installation process, LEDs active.

Fig. 2.   Illustration of URPIS usage concept with multirotor system consisting of (a) target search, (b) wall contact, (c) resin dispersal and curing, (d) payload release and detachment.

ACT combines ideas of contact-based release with mechanical adhesion from *C. Hirsuta* and *A. quandang* into a single 3D-printed structure for ease of handling. Dispersal of liquid UV resin is triggered via the IM, responsible for fracturing the ACT against a target surface.

Deployment with multirotors is envisioned as a 4 stage process in Fig. 2: (a) target search, (b) wall perching (c) resin curing and (d) payload release. During (a), a suitable installation surface is identified and approached with the multirotor. On successful wall contact and perching (b), resin dispersal (c) starts with a spring-driven impactor fracturing the resin-filled ACT against the target surface. UV LEDs behind the ACT cure the dispersed resin in 10 seconds, before the payload (d) is released. The process ends with the multirotor detaching from the ACT and un-perching itself from the wall, leaving the installed payload behind.
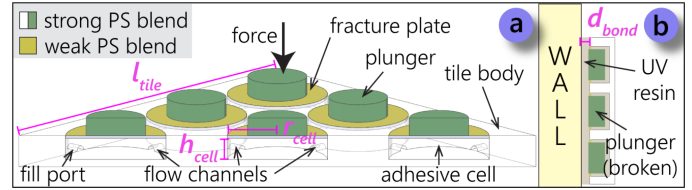

Fig. 3.   (a) Dimetric cross-section view of ACT before impact, (b) side cross-section view of ACT after fracturing and dispersing resin.

B. System Design Goals

To address limitations of current works on aerial payload installation, authors sought solutions with these design goals:

- It must be deploy-able on large surfaces and across varying material types and roughness.
- It should provide the payload a strong, robust and permanent connection to the installation target.
- It must have a scalable design that is easy to manufacture, integrate and use on multirotors.

C. Key Design Decisions

1) Use of UV-Curable Wet Adhesives: UV-curable wet adhesives were selected for its excellent adhesion performance, low curing energy requirements and rapid-curing abilities. They do not require power to maintain adhesion after curing, and are also less-affected by surface contaminants in experiments. In contrast, active suction [9] requires considerable power and smooth, non-porous surfaces, dry adhesives lose potency with surface contaminants and mismatched surface roughness, and electrostatic systems require smooth non-conductive surfaces [16] [17]. Dymax 1406 M, a urethane acrylate type UV adhesive (385 nm–405 nm) was selected for its fast-curing and low-viscosity (150 cP) properties.

2) Use of Multi-Material 3D Printing for ACTs: Multi-material 3D printing affords targeted material placement, manufacturing of internal cavities and design freedom for functional geometry in a single part. It beneficially reduces component count and moving parts whilst improving ease-of-handling, thus simplifying manufacturing and usage.

3) Impact-Based Trigger for Resin Dispersal: Using impact is advantageous on multirotor systems, as it keeps sustained reaction force requirements low whilst ensuring quick resin dispersal on the target. It also exploits the brittleness of polystyrene, a material chosen for its UV transparency.

III. ADHESIVE CARRIER TILE (ACT) DESIGN

A. ACT Design Features

Multi-material 3D-printing is employed to create the ACT, a single-part structure designed to store and release UV liquid resin on impact. It is a single-use consumable that can be easily loaded onto aerial platforms. Several features of the ACT (see Fig. 3) enable its intended function:

- A polystyrene (PS) structure that is transparent to UV light for curing adhesives.
- A fracture layer using a weaker 70:30 PS blend that lowers impact forces required for fracture.
- Plunger-like structures on the ACT's impact face that break through the weakened layer to displace resin.

- Internal adhesive cell cavities for storing UV resin prior to dispersal via impact.
- Fill ports and flow channels between cell cavities for filling the ACT with UV resin using a needle.

B. ACT Modelling and Design Parameters

Each ACT consists of several resin-filled cells. Force F_{cell} required for rupturing each cell is described in (1) obtained from [18]. The permissible load borne by each cell W_{cell} depends on contact area $A_{contact}$ and maximum shear stress $\tau_{surface}$ at the bond interface (see (2)), where $A_{contact}$ is obtained from cell volume V_{cell} in (3) assuming uniform bond depth d_{bond}, subject to printer bridging length capability r_{limit}. Achieving target load W_{target} is a matter of scaling cell quantity n (see (4)).

$$F_{cell} = \sigma_{max}(2.814\pi t_{cell}^2) \tag{1}$$

$$W_{cell} = \tau_{surface} A_{contact}, \text{ where } A_{contact} = \frac{V_{cell}}{d_{bond}} \tag{2}$$

$$V_{cell} = \pi r_{cell}^2 h_{cell}, \text{ s.t. } 0 \le r_{cell} \le r_{limit} \tag{3}$$

$$n = \text{ceiling}\left(\frac{W_{target}}{W_{cell}}\right) \tag{4}$$

IV. ACT FABRICATION AND CHARACTERISATION

A. ACT Fabrication Materials and Methods

1) Polystyrene Filament Production: Given the lack of commercial polystyrene (PS) filaments, 1.75 mm PS filament was extruded directly from pellets using 3devo's Filament Maker Composer at 220 C (Fig. 4(a)), enabling polymer blending for tailored material properties. 192 k and 45 k molecular weight (MW) PS pellets were combined in a 70:30 ratio for the weaker fracture plate ($\sigma_{max} = 23 \pm 3$ MPa), while pure 192 k MW pellets were used for the plungers and tile body ($\sigma_{max} = 51 \pm 7$ MPa).

2) 3D Printing Process Parameters: ACTs were produced on a dual independent extruder (IDEX) printer to incorporate the weaker fracture plate into the rest of the structure for controlled failure. The hotend and bed temperatures were set to 220 C and 120 C respectively, with the ACT printed at 0.1 mm layer height. A glass bed was used to obtain a smooth bottom finish for improved UV light transmission.

3) ACT Filling Procedure: The ACT contains a 3-by-3 grid of cylindrical voids, linked together by flow channels (Fig. 3(a)). It requires drilling out a fill port, through which a needle is inserted for loading UV resin. Gaps between the needle and port allow air to bleed out, while flow channels allow all cells in the ACT to be filled with 1 port. Surface tension prevents the adhesive from leaking out of filled ACTs. Each ACT takes 60 s to fill completely, before being stored in an opaque container.

B. ACT Characterisation Experiments

1) ACT Plunger Fracture Force: (1) predicts a typical fracture force of 18.3 N ($\sigma_{max} = 23$ MPa) for plate thickness $t = 0.3$ mm per cell. It was experimentally found to be 18 ± 3 N via a universal testing machine (UTM) from Instron.

2) UV Transmission Efficiency: Tests were conducted with a UV intensity meter held 10 mm away from a calibrated UV light source to determine transmission losses from passing through
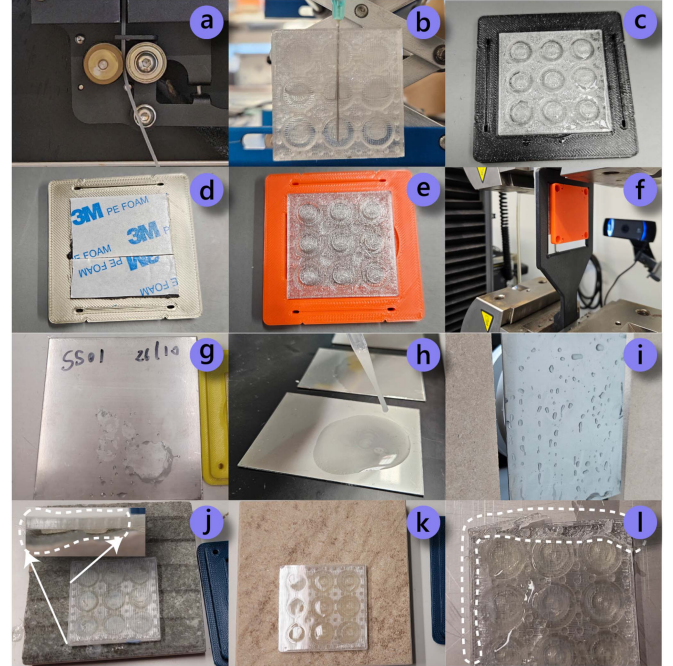

Fig. 4. (a) Making custom 1.75 mm PS filament, (b) process of filling ACT with resin using needle, (c) fractured ACT with uncured UV resin on surface, (d) blank tile with foam tape (control), (e) UV resin-filled ACT, (f) sample undergoing tensile testing, (g) stainless steel test surface, (h) preparation of steel plate with talcum powder IPA suspension, (i) wet stainless steel test surface, (j) ridged cermamic test surface with side view, (k) smooth ceramic test surface, (l) ACT delamination failure.

the ACT. UV transmission efficiency of 41% was obtained with a Silverline UV radiometer.

3) UV Cure Time: Gravimetric experiments were conducted using viscosity as a measure of cure state. Samples of Dymax 1406 M adhesive were pulsed with measured doses of UV energy at fixed intervals, then measured using viscometry. Between 0 s to 8 s, it was observed UV resin achieved partial cure. Full hardening of the adhesive was only achieved after 10 s @ 100 mW/cm^2. It was also observed that Dymax 1406 M had an upper bound of 200 mW/cm^2 for UV absorption, beyond which no improvement in cure rate was observed. While the influence of temperature was not studied, a positive relationship between higher temperatures and resin cure rates was established in [19].

4) Adhesion Force Characterisation: Shear strength experiments comparing general-purpose dry adhesive (3 M 1600 T PE foam tape) against Dymax 1406 M UV resin were performed to evaluate adhesion performance across a variety of common building materials and surface conditions. Dry-adhesive samples were tested immediately after application to replicate initial strength prior to loading. Prepared samples (Fig. 4(d) and (e)) were then evaluated via Instron tensile tester, with tests were repeated thrice to obtain average maximum load capacity (see Fig. 5).

Dry, wet and dusty stainless steel plates were prepared, with wet conditions replicated using a spray bottle, while dust was introduced using 1ml of isopropanol talcum powder suspension (20 mg/ml) in Fig. 4(h). ACTs reached a maximum of 915 ± 46 N before failure on dry stainless steel. Notably, UV resin remained unaffected by wet surfaces, with shear strength remaining within 2.1% of dry steel plates. Introducing large
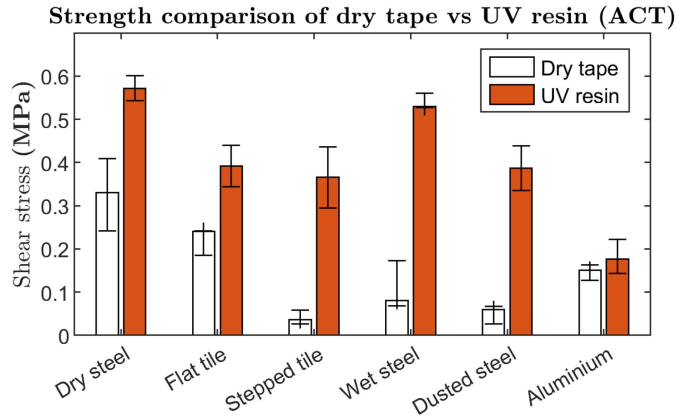
Fig. 5. Strength comparison between dry tape and wet adhesives across steel, aluminium and ceramics with varied surface conditions.
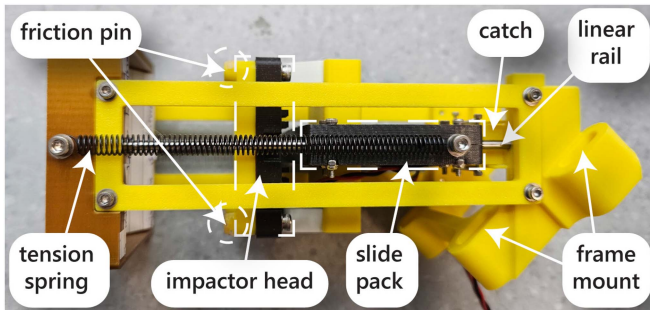

Fig. 6. Diagram of impactor mechanism components after priming.

amounts of simulated dust was necessary to induce a strength loss of 32.3%.

Rough ceramic tiles of assorted surface geometries (flat and stepped) were used to investigate the effects of surface roughness on adhesion performance. Tests using stepped ceramic tiles yielded the largest difference in shear strength. Unlike the UV resin which conforms to the surface (see Fig. 4(j)), the effective contact area for dry tape was much lower, resulting in a 10.2x reduction in shear strength.

Lastly, aluminium plates were included to study the effects of a passivation layer on adhesion. In general, aluminium was an outlier, with the ACT sample failing at just 282 ± 53 N, 3.2x lower than dry stainless steel. Notably, the performance of dry tape was somewhat comparable, with UV resin only outperforming dry tape by 16.6% in shear strength.

The primary failure mode for steel was delamination (see Fig. 4(l)) of the ACT as opposed to the adhesive itself, suggesting that bond strength was not the limiting factor. A structural re-design of the tile to include thicker part wall geometry, or the use of stronger PS (higher MW) could yield further improvements in maximum loading.

V. IMPACTOR MECHANISM (IM) DESIGN

A. Impactor Mechanism Details

The impactor mechanism is supported by a rigid frame (see Fig. 6), serving as a mechanical interface between the multirotor and enabling force transmission from the impactor head into the
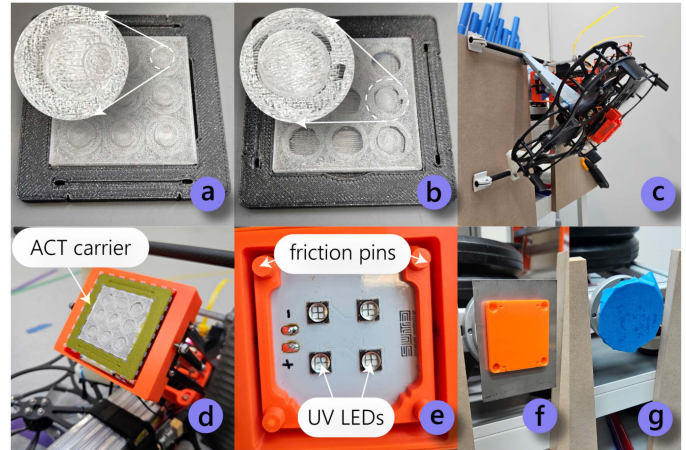

Fig. 7. (a) Close-up of intact ACT, (b) close-up of fractured ACT, (c) multirotor test platform perched on impact measurement rig, (d) view of impactor with ACT loaded, (e) close-up of impactor head with UV curing subsystem, (f) stainless steel tile dry tape sample on impact measurement sensor, (g) impact measurement sensor covered in protective tape layer.

target surface. It is mostly 3D-printed, apart from the use of metal fasteners, rails and springs.

Within the rigid frame lies the linear motion system, consisting of the impactor head, slide pack and servo-driven catch. The impactor head is mounted fore of the slide pack, and houses the UV curing subsystem with friction pins for mating to the ACT. The slide pack consists of 4 linear bearings on 3 mm linear rails, accelerated by a pair of 8 mm tension springs that are primed prior to takeoff. When perched and ready, a servo-driven catch opens, releasing the slide pack and impactor head into the target surface, where the ACT fractures on impact for resin dispersal. In total, the impactor mechanism weighs 288 g, with a moving mass (impactor head, slide pack) of 108 g.

The impactor also houses a UV subsystem (Fig. 7(e)) for adhesive curing, composed of a 2×2 grid of 385 nm UV LEDs placed behind the ACT, powered by a Stratus LumiBoost LED driver and calibrated to an intensity of 150 mW/cm^2. Surface-mount LEDs are placed on a copper board for heat dissipation.

B. Impactor Mechanism Modelling

The impactor mechanism drives the ACT into the target surface, pushing plungers through the fracture plate and dispersing resin onto the target surface. Average impact force F_{avg} must exceed the combined fracture force requirements for all cells in the configured ACT (see (5)). The recoil generated by a spring-driven impactor depends on k and spring displacement d_h subject to size constraints d_{limit} (see (6)), assuming negligible friction.

$$F_{avg} = \frac{m_h v^2}{2h_{cell}}, \text{ s.t. } F_{avg} \geq nF_{cell} \tag{5}$$

$$F_{recoil} = kd_h, \text{ s.t. } 0 \leq d_h \leq d_{limit} \tag{6}$$

C. Impactor Characterisation Experiments

A PCB Piezotronics 208C03 impact sensor (Fig. 7(g)) was used to profile impactor force over time. To replicate operating conditions, a loaded multirotor was perched onto a cart with the
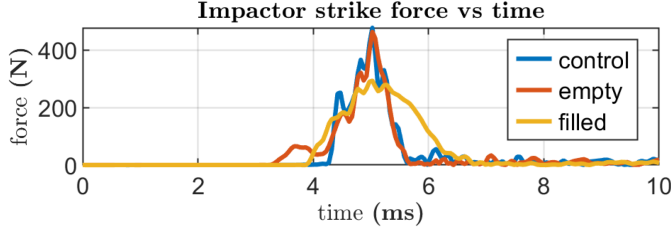
Fig. 8. Force-time measurements experienced by the tile for blank, empty and filled tiles.

sensor under its own thrust in Fig. 7(c). Blank, unfilled and filled tiles were tested to examine potential damping effects from tile fracture and fluid ejection. Fully-charged (4.2 V/cell) lithium-polymer (LiPo) batteries were used for each tile set to account for voltage-related thrust effects.

Force-time graphs from each tile type were averaged, before being fed through a Savitzky-Golay (order 7, length 11) smoothing filter to reduce noise while preserving peak data. Fig. 8 shows peak force readings from blank, unfilled and filled ACTs. Blank tiles were highest at 480 N, with unfilled and filled ACTs at 450 N and 293 N respectively. Filled ACTs saw a 39% decrease in peak force due to fluid damping effects, which still exceeds the $F_{\mathrm{avg}} = 162 \mathrm{~N} \pm 27 \mathrm{~N}$ required for fracture (for $n = 9$), but must be accounted for in impactor design.

VI. WALL BRACE DESIGN, PERCEPTION AND PERCH CONTROL

A. Wall Brace Implementation

A passive wall brace system prevents the multirotor from slipping on the wall during perching, helps position URPIS at the appropriate distance and also mounts L515 LiDAR camera. It consists of front and rear tube clamps, spanned by carbon rods with foot pads. Pliable grip tape (3M GM641) applied to the foot pads improves contact friction required for slip-free wall perching.

B. Wall Brace Modelling

The wall brace maintains the multirotor's grip on the target surface while perched, keeping the vehicle static for effective tile curing. Fig. 9 shows the forces acting on the multirotor. θ_{perch}, c, μ, l_{h}, throttle setpoint b are tweaked to ensure that directed thrust T_1 and T_2 remains sufficient to resist recoil from the impactor's operation while also supporting the craft's weight. Assuming T_1 and T_2 are symmetrical, maximum thrust T_{max} is used to derive perch thrust T_{perch} in (7). Checks to satisfy horizontal, vertical and torque forces are defined in (8), (9), (10) and (11).

$$T_{\mathrm{perch}} = bT_{\mathrm{max}}cm_{\mathrm{c}}g \tag{7}$$

$$F_{\mathrm{x}} = T_{\mathrm{perch}}sin\theta - kd_{\mathrm{h}} \geq 0 \tag{8}$$

$$F_{\mathrm{y}} = T_{\mathrm{perch}}cos\theta - m_{\mathrm{c}}g - R_{\mathrm{y}} \leq 0 \tag{9}$$

$$R_{\mathrm{y}} = \max(0, \mu(F_{\mathrm{x}})) \tag{10}$$

$$\tau_{\mathrm{z}} = l_{\mathrm{t}}T_{\mathrm{perch}} - l_{\mathrm{c}}m_{\mathrm{c}}g - l_{\mathrm{h}}F_{\mathrm{recoil}} \geq 0 \tag{11}$$

The transition from hover to perched mode is modelled with the hinge-pin assumption, where (12) and (13) represent contact forces and (14) represents torque acting about the pivot point
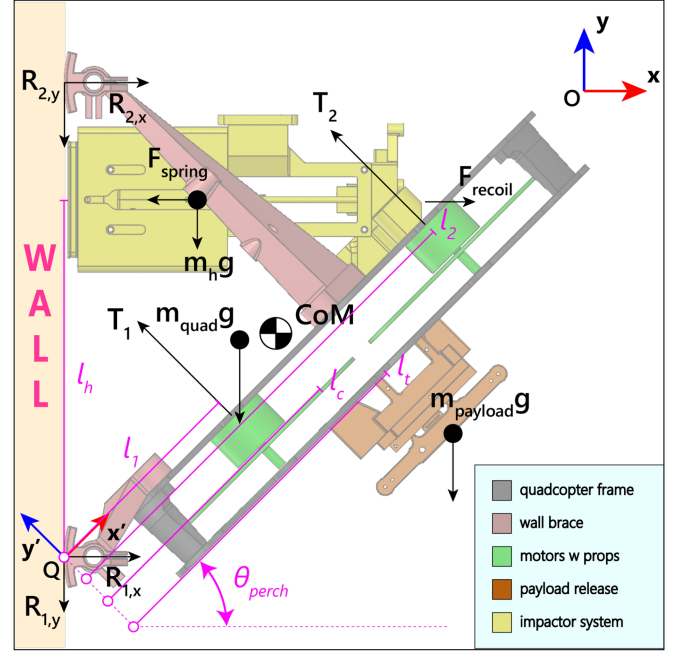

Fig. 9. Free body diagram of forces acting on multirotor airframe.

transitioning from hover flight to a stable perch.

$$T_{1\mathrm{x}} + T_{2\mathrm{x}} + R_{\mathrm{x}} = 0 \tag{12}$$

$$T_{1\mathrm{y}} + T_{2\mathrm{y}} + T_{\mathrm{y}} = 0 \tag{13}$$

$$I\ddot{\theta} = mgl_{\mathrm{c}} + T_1l_1 + T_2l_2 \tag{14}$$

C. Wall Surface Detection and Alignment Algorithms

An onboard RealSense L515 LiDAR provides front-facing 3D point-cloud data feeding wall and flatness detection algorithms. Wall detection and alignment is implemented using the standard random sampling & consensus (RANSAC) algorithm [20] for obtaining a best-fit plane and normal vector for alignment.

For a target wall to be suitable, it must be sufficiently flat, and also fit the multirotor's perched footprint. Wall flatness within a small region of interest (ROI) corresponding to the airframe's footprint is considered. A ratio is taken (see (15)) from the set of points M within the ROI; P_{perch} must exceed a predefined threshold for a target to be "perch-able".

$$P_{\mathrm{perch}} \overset{\mathrm{def}}{=} \frac{\sum_{k=1}^{M} \hat{D}_k}{M}, \text{ where } M \subset N \tag{15}$$

D. Contact and Perching Control

1) Contact Detection: Contact sensing is used in-lieu of depth data when under the L515's minimum working range, implemented as onboard thresholding of IMU readouts (see (16)). This approach also verifies the identified target surface is firm enough for payload installation.

$$|A_{\mathrm{hit}}| \geq |A_{\mathrm{firm}}|, \text{ where } |A_{\mathrm{hit}}| = \sqrt{A_{\mathrm{x}}^2 + A_{\mathrm{y}}^2} \tag{16}$$

2) Perching Controls: Transitioning from hovering to perching is achieved using the determined θ_{perch} as a pitch setpoint via the onboard flight controller. Throttle value b is used during the

TABLE I
SYSTEM PARAMETERS

ACT parameters	Value
Plunger height, h_{cell}, d_h (mm)	3.0
Bond depth, d_{bond} (mm)	1.0
Fracture layer thickness, t_{cell} (mm)	0.30
ACT length, l_{length} (mm)	40.0
Surface adhesion strength, $\tau_{surface}$ (MPa)	3.5 ± 0.4
Neat PS flexural strength, σ_{max} (MPa)	51 ± 7
70:30 PS flexural strength, σ_{max} (MPa)	23 ± 3
Impactor parameters	**Value**
Impactor moving mass, m_h (kg)	0.108
Spring constant, k (N/m)	400
Impact distance, d_h (mm)	3.0
Multirotor parameters	**Value**
Max. thrust, T_{max} (kg)	4.64
Thrust-to-weight ratio, c	2.23
System mass, m_c (kg)	2.06
System CoM position (x', y'), $\vec{r_{CoM}}$ (m)	0.16, 0.02
Friction coefficient, μ	1.6
Final perch angle, θ_{perch} (deg)	46.4
Thrust setpoint, b_{hover}, b_{impact}, $b_{unperch}$	0.42, 0.7, 0.35
Airframe characteristic length, l_f (m)	0.5
Impactor relative position, l_h	0.8
Perchability threshold, P_{perch}	0.95
Contact acceleration threshold, A_{firm} (m/s^2)	6.0

initial perch. Post-release of impactor, throttle setpoint values b_{hover} and b_{torque} are derived from prior (7) to satisfy (8), (9), (10) and (11), yielding un-perching throttle setpoints in (17) and (18).

$$b_{hover} = \frac{l_c}{l_t c T_{max}} \qquad (17)$$

$$b_{torque} = \frac{1}{c T_{max} cos(\theta_{perch})} \qquad (18)$$

$$b_{unperch} = \min(b_{torque}, b_{hover}) \qquad (19)$$

For un-perching, the multirotor exploits its own mass m_c to detach itself from the wall's surface. Changes in pitch θ are used as a substitute for feedback. Un-perching is accomplished by reducing throttle setpoint to $b_{unperch}$ until a change ϵ pitch angle is observed, taken as separation from the surface and ACT. The removal of contact forces acting on the multirotor's body permits a return to regular hover flight. A ramp function in (20) gradually reduces the throttle setpoint b until detachment occurs.

$$b = \begin{cases} \max(-gt + 1.0, b_{unperch}), & \text{if } \theta \geq \theta_{perch} - \epsilon \\ b_{hover}, & \text{otherwise} \end{cases} \qquad (20)$$

VII. MULTIROTOR SYSTEM DETAILS

A. Platform Specifications, Parameters and Operating Points

The multirotor uses a QAV-PRO Whoop 5" Cinequads Edition frame, mated to four T-Motor F90 KV1300 motors. A PX4 flight controller [21] handles flight functions, together with a LattePanda companion computer for offboard control, datalinks and vision processing algorithms, as well as an Intel RealSense L515 camera for point cloud data. Payload release, UV curing and resin dispersal subsystems are triggered remotely. Refer to Fig. 10 for an overall picture.

System parameters are listed in Table I. The multirotor requires a theoretical thrust setpoint of $b = 0.338, 0.92$ and 0.398 for unperching, impactor deployment and hover respectively. In
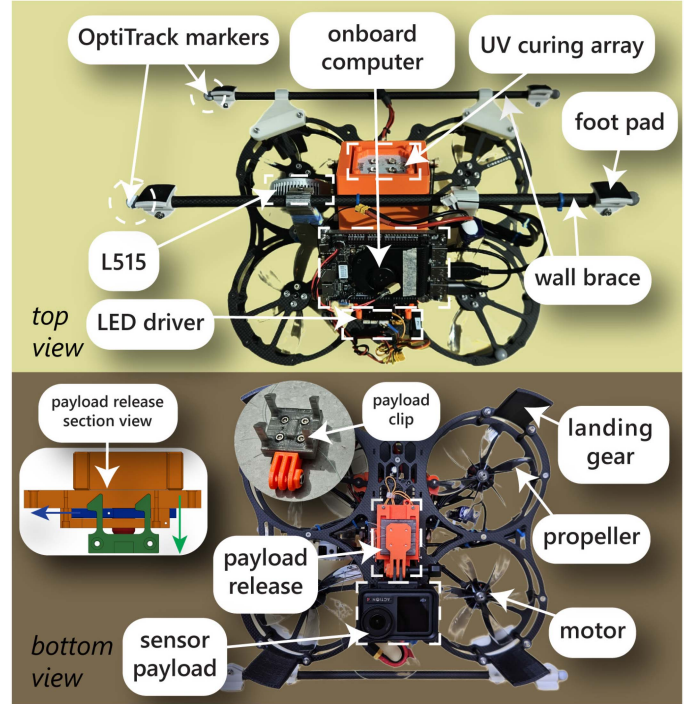

Fig. 10. Overall diagram featuring main subsystems on test platform.

practice, similar setpoint values $b = 0.35, 0.7$ and 0.42 remain viable, with the frame imperceptibly lifting off the wall due to recoil from impactor release. Astute readers will notice the parameter l_h selected in Fig. 11-3 falls outside the feasible region for fully-static perching; this is due to physical constraints of the chosen frame. In practice, the slight lifting does not present any issues for ACT fracture.

B. Payload Install Procedure

On take-off, the multirotor ascends to the target altitude and begins its search for a best-fit plane within field-of-view resembling a wall section. Once found, the multirotor yaws itself in alignment with the plane and commences searching for a suitably-flat surface, by translating along the plane's surface till satisfaction of the flatness criterion, at which point the wall perching process begins. Then, the multirotor approaches a setpoint on the target surface as identified by the camera. After confirmation of wall contact using a combination of IMU-based contact sensing and range readouts, it then transitions into attitude control for perching, resin dispersal, curing and payload release. On completion of payload installation, the multirotor switches to unperching control logic that uses body pitch angle and LiDAR ranging to determine the state of unperching. Once free from the wall, the multirotor returns to position control before landing. The installation process is summarised in Fig. 12.

VIII. INSTALLATION EXPERIMENTS & ANALYSIS

A. Installation Experiment Setup

Installation experiments were conducted in an indoor flying space to utilise existing walls. A section of plaster wall served as a target surface, flanked by pool noodles for simulating infeasible deployment areas (approx. 3 cm depth) for the L515 camera.
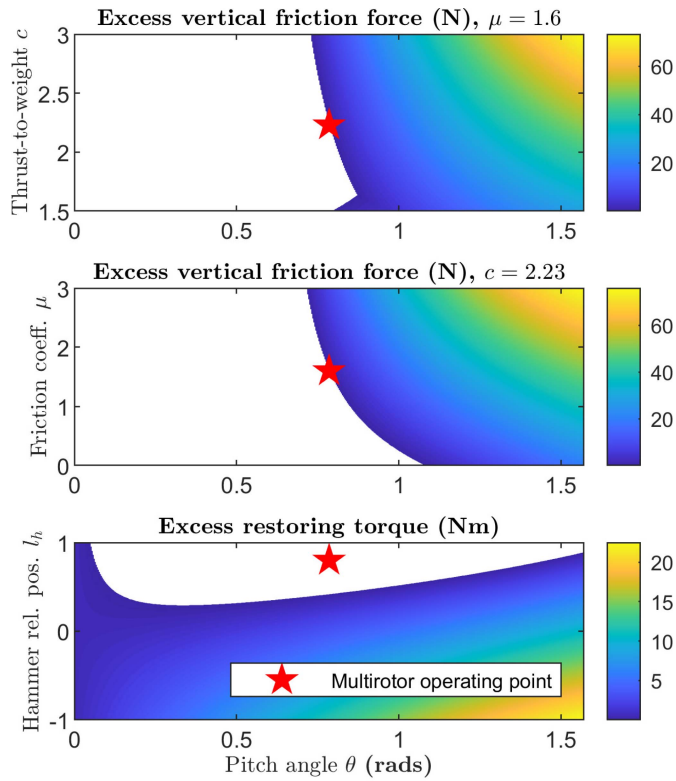
Fig. 11. Contour plots varying θ_{perch} and system parameters c, μ and l_h (Table I), showing ability resist slippage and torques while perched, derived from wall brace modelling. Feasible regions are coloured and the operating point for experimental multirotor is marked in green.
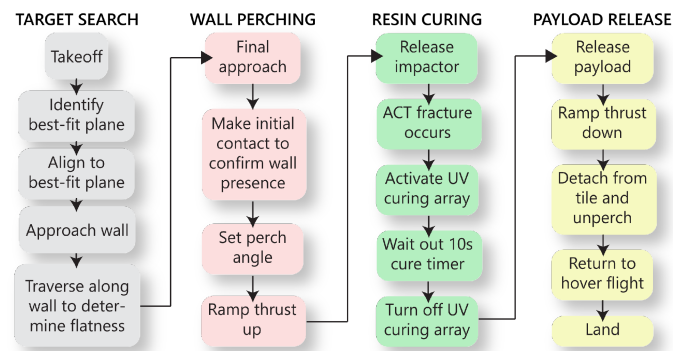

Fig. 12. Process diagram of payload installation experiment.

Feasible deployment areas were covered with painter's tape in order to protect the underlying paint surface (Fig. 13). Position estimates were obtained via an OptiTrack motion capture system in lieu of GNSS typically available for outdoor flights. Guidance and navigation post-wall detection leveraged the L515 camera and onboard flight controller. The process is fully-automated, with no pilot input required apart from mode-switching to start the experiment.

B. Perching Experiments

Craft attitude was tracked using a combination of onboard inertial and motion-capture data. Data obtained from the
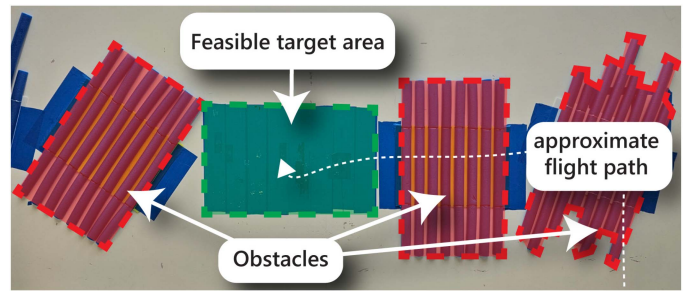

Fig. 13. Testing area for payload installation experiment; pool noodles simulate infeasible areas (red), while flat area with painter's tape feasible for installation (green).
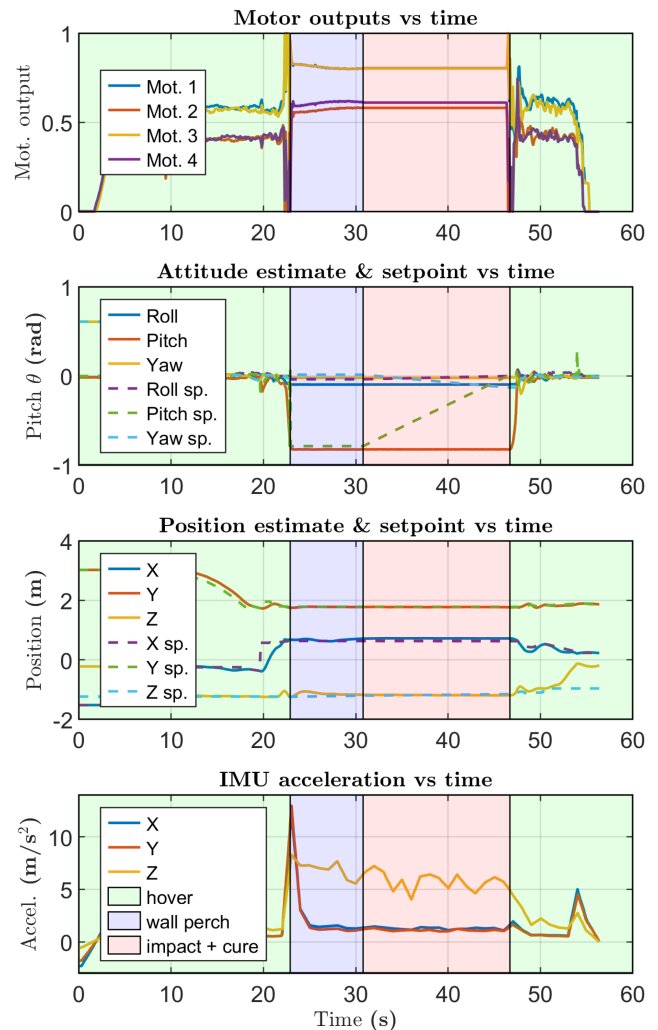
Fig. 14. Flight logs of (1) motor output, (2) attitude, (3) position and (4) acceleration.

flight controller including multirotor attitude, position, commanded pitch, thrust output and and commanded thrust setpoints was studied to determine the suitability of control outputs from PX4.

Referring to position and attitude plots (Fig. 14-3 & 4), the setpoints were generally well-tracked. In flight, the front-heavy CoM manifests as motor output differences (Fig. 14-2) during

hover and perching, with the front output value 0.2 higher than rear motors. When perched, differences between the desired setpoints and pose were correlated with lopsided actuator outputs from PX4's mixer logic. For instance, small yaw errors manifested as differences in output from rear motors 2 and 4 (Fig. 14-1). The inherent stability of the multirotor during impact and perching segments is represented by invariant position and attitude values in Fig. 14-2 and 3, as well as the stable pitch values despite the changing pitch setpoint. Onboard IMU data plots show the contact detector threshold of 6.0 G working as intended (see Fig. 14-4).

C. Sensor Payload Installation

An action camera payload is secured to the ACT using nylon tether (see Fig. 10), intended to replicate a real-world payload installation task. The process is fully-automated apart from mode-switching to initiate takeoff. Refer to the video for recorded footage from the payload's perspective.

D. Overall System Limitations

The design of the wall brace and flight motor configuration limits perching to hard near-vertical surfaces. Experiments indicate that minor variations in perch angle are tolerable; the test setup errs from true vertical by ± 5 degrees. However, URPIS will continue to function regardless of orientation as long as sufficient reaction force exists to fracture the ACT.

Factors such as exposure of the uncured ACT to strong direct sunlight will cause URPIS to fail, as UV exposure will increase the resin's viscosity and therefore the F_{avg} for fracture. The UV resin must be exposed to the full curing (>10 s) duration to reach maximum strength. In addition, factors that reduce the adhesive's contact area $A_{contact}$ such as surface irregularities (roughness >2 mm), curvature or partial ACT fracture will lower the maximum achievable W_{cell}.

IX. CONCLUSION

This letter demonstrates the viability of URPIS on a multirotor without additional flight actuators. The main advantages conferred by using wet over dry adhesives or magnets lie in (1) its applicability across varied surface conditions, (2) load bearing capacity and (3) bond permanence. In addition, low continuous force requirements even permit small aerial vehicles to perform payload installation tasks. Future works to adapt the platform and URPIS for other surface types could leverage compliant tile segments that better conform against the surface, or re-configurable bracing morphologies that allow multirotors to generate the requisite reaction forces against non-vertical surface targets.

REFERENCES

[1] K. C. Vaughn, A. J. Bowling, and K. J. Ruel, "The mechanism for explosive seed dispersal in Cardamine hirsuta (Brassicaceae)," *Amer. J. Botany*, vol. 98, no. 8, pp. 1276–1285, Aug. 2011.

[2] D. L. Chothani, M. Patel, S. Mishra, and H. Vaghasiya, "Review on Ruellia tuberosa (cracker plant)," *Pharmacognosy J.*, vol. 2, no. 12, pp. 506–512, Aug. 2010.

[3] J.-i. Azuma, N.-H. Kim, L. Heux, R. Vuong, and H. Chanzy, "The cellulose system in viscin from mistletoe berries," *Cellulose*, vol. 7, no. 1, pp. 3–19, 2000.

[4] M. A. Estrada, S. Mintchev, D. L. Christensen, M. R. Cutkosky, and D. Floreano, "Forceful manipulation with micro air vehicles," *Sci. Robot.*, vol. 3, no. 23, Oct. 2018, Art. no. eaau6903.

[5] I. Armengol, A. Suarez, G. Heredia, and A. Ollero, "Design, integration and testing of compliant gripper for the installation of helical bird diverters on power lines," in *2021 IEEE Aerial Robot. Syst. Phys. Interacting With Environ.*, 2021, pp. 1–8.

[6] R. Lim, K. Lim, and S. Foong, "Design and analysis of a gravitic tether-based grappler for aerial payload deployment," in *2022 IEEE/ASME Int. Conf. Adv. Intell. Mechatron.*, 2022, pp. 695–702.

[7] M. Zhao, K. Nagato, K. Okada, M. Inaba, and M. Nakao, "Forceful valve manipulation with arbitrary direction by articulated aerial robot equipped with thrust vectoring apparatus," *IEEE Robot. Automat. Lett.*, vol. 7, no. 2, pp. 4893–4900, Apr. 2022.

[8] Y.-H. Hsiao et al., "Energy efficient perching and takeoff of a miniature rotorcraft," *Commun. Eng.*, vol. 2, no. 1, Jun. 2023, Art. no. 38.

[9] Y.-w. Song et al., "Development of safety-inspection-purpose wall-climbing robot utilizing aerial drone with lifting function," in *2021 18th Int. Conf. Ubiquitous Robots*, 2021, pp. 411–416.

[10] T. Kim, B. Yu, C. Tirtawardhana, I. M. A. Nahrendra, and H. Myung, "Development of cleaning module for wall climbing drone with bio-inspired watering mechanism," in *2022 22nd Int. Conf. Control, Automat. Syst.*, 2022, pp. 1432–1436.

[11] R. Mattar and R. Kalai, "Development of a wall-sticking drone for non-destructive ultrasonic and corrosion testing," *Drones*, vol. 2, no. 1, Feb. 2018, Art. no. 8.

[12] M. Rossi, D. Brunelli, A. Adami, L. Lorenzelli, F. Menna, and F. Remondino, "Gas-drone: Portable gas sensing system on UAVs for gas leakage localization," in *Proc. IEEE SENSORS 2014 Proc.*, 2014, pp. 1431–1434.

[13] C. Ding, L. Lu, C. Wang, and C. Ding, "Design, sensing, and control of a novel UAV platform for aerial drilling and screwing," *IEEE Robot. Automat. Lett.*, vol. 6, no. 2, pp. 3176–3183, Apr. 2021.

[14] R. Dautzenberg et al., "A perching and tilting aerial robot for precise and versatile power tool work on vertical walls," in *2023 IEEE/RSJ Int. Conf. Intell. Robots Syst.*, Detroit, MI, USA, 2023, pp. 1094–1101.

[15] C. H. Tan, K. Hölttä-Otto, and S. Foong, "Efficient design guidelines for innovative aerial robot design," *J. Mech. Des.*, vol. 144, no. 11, Jul. 2022, Art. no. 111403.

[16] R. Sahay, H. Y. Low, A. Baji, S. Foong, and K. L. Wood, "A state-of-the-art review and analysis on the design of dry adhesion materials for applications such as climbing micro-robots," *RSC Adv.*, vol. 5, no. 63, pp. 50821–50832, 2015.

[17] M. F. Silva, J. A. T. Machado, and J. K. Tar, "A survey of technologies for climbing robots adhesion to surfaces," in *2008 IEEE Int. Conf. Comput. Cybern.*, 2008, pp. 127–132.

[18] W. C. Young and R. G. Budynas, *Roark's Formulas for Stress and Strain, (McGraw-Hill International Edition, General Engineering Series)*, R. J. Roark, Ed., 7th Ed. New York, NY, USA: McGraw-Hill, 2011, ch. 11, pp. 427–524.

[19] B. Golaz, V. Michaud, Y. Leterrier, and J.-A. Månson, "UV intensity, temperature and dark-curing effects in cationic photo-polymerization of a cycloaliphatic epoxy resin," *Polymer*, vol. 53, no. 10, pp. 2038–2048, Apr. 2012.

[20] K. G. Derpanis, "Overview of the RANSAC algorithm," *Image Rochester NY*, vol. 4, no. 1, pp. 2–3, 2010.

[21] L. Meier, D. Honegger, and M. Pollefeys, "Px4: A node-based multi-threaded open source robotics framework for deeply embedded platforms," in *2015 IEEE Int. Conf. Robot. Automat.*, May 2015, pp. 6235–6240.